A COUPLED TEMPERATURE-MICROSTRUCTURE MODEL FOR THE HEAT-AFFECTED ZONE OF LOW ALLOYED HIGH STRENGTH STEEL DURING TWO-PASS ARC WELDING

J. PAANANEN *, A. POHJONEN*, J. LARKIOLA* and S. ANTTILA**

**University of Oulu, Materials and Production Technology, Pentti Kaiteran katu 1, 90014 Oulu, Finland, firstname.lastname@oulu.fi*
***SSAB Europe, P.O. Box 93, 92101 Raahe, Finland, firstname.lastname@ssab.com*

DOI 10.3217/978-3-85125-615-4-15

ABSTRACT

A coupled temperature-microstructure model was developed in order to simulate the evolution of the microstructure in the heat-affected zone during two-pass gas-metal arc welding. The model is developed to serve the steel industry's need to evaluate the weldability of new steel grades. Heat transfer and heat input models were used for modelling the arc welding and the temperature changes in the heat-affected zone. A microstructure model was fully coupled with the temperature model, including latent heat of transformation as well as the dependence of thermophysical properties on temperature and phase fractions. The microstructure model simulates phase transformations and grain growth including a simplified model for the effect of fine particles. The modeled temperature paths are in good agreement with the measured ones. The final phase fractions and grain size distribution obtained from the model correspond to the actual microstructure and the model predicts the shapes of the heat-affected zone and fusion zone with relatively good accuracy.

Keywords: Microstructure, Phase Transformations, Grain Growth

INTRODUCTION

There is a need in the steel industry to shorten the steel development cycle to meet the increasing customer demands. Therefore, weldability models that can predict the microstructure evolution without real welding experiments would help to achieve this goal. Modelling can also give valuable information of the microstructure evolution that is difficult or impossible to obtain experimentally. Although feasible welding models have

been developed in the past, the increase in computational power has made it possible to create more detailed models and still maintain relatively low calculation times.

Goldak et al. [1] developed a model that predicts the heat flow in welds. They used a non-linear heat equation to take into account the effect of temperature on thermal conductivity and specific heat capacity. The authors presented two and three-dimensional approaches and were able to get a good agreement between the experimental and modelled results.

Watt et al. [2] developed quite comprehensive algorithm for the evolution of microstructure. Their model predicts the final microstructure, the phase fractions and the grain size, based on chemical composition of the steel. Henwood et al. [3] verified the algorithm in their paper. However, there were some aspects that were simplified. For instance, the authors assumed that austenitization occurs near equilibrium conditions and that the grain growth occurs only after the particles have dissolved. In addition, they assumed that after reaching the martensite start temperature the remaining austenite will transform into martensite.

The model presented in this paper includes a heat transfer model for the conduction in the steel, convection and radiation at the surfaces and the heat input from the arc. The heat transfer model is fully coupled with a microstructure model that includes phase transformations, grain growth and a rough model for precipitates. The paper aims to bring some new aspects on weldability modeling and overcome some of the drawbacks of the earlier methods. For example, the grains may grow in the presence of pinning particles. The phase transformation model is based on experiments and it for instance, allows simultaneous decomposition of austenite to ferrite, bainite and martensite and the grain growth in the presence of pinning particles. In addition, the thermophysical properties are functions of temperature and present phase fractions.

DESCRIPTION OF THE MODEL

Due to high temperature gradients together with high heating and cooling rates that exist in actual welds, very fine grid and short time step are required. Therefore, it was a necessity to reduce the calculation time by using a two-dimensional model. The dimension where the temperature gradient was assumed to be zero was the direction of the movement of the torch as in Fig 1. Obviously, this was a very rough assumption. However, the results to be presented show that the used two-dimensional approach gave reasonable accuracy. Goldak et al. [1] also showed that two dimensional approach is sufficient for points far from the heat source for high speed productive welds in steel. The presented model is intended for the heat-affected zone and only little attention is paid on fusion zone phenomena. Thus, it is assumed that the points in the heat-affected zone are sufficiently far from the heat source but the accuracy of the temperature model in the fusion zone may not be sufficient. The model also assumes that inter-critical zones behave as the fully austenitized zones. This may not hold true in all cases and therefore, this model may not be suitable for the microstructure of inter-critical heat-affected zone.

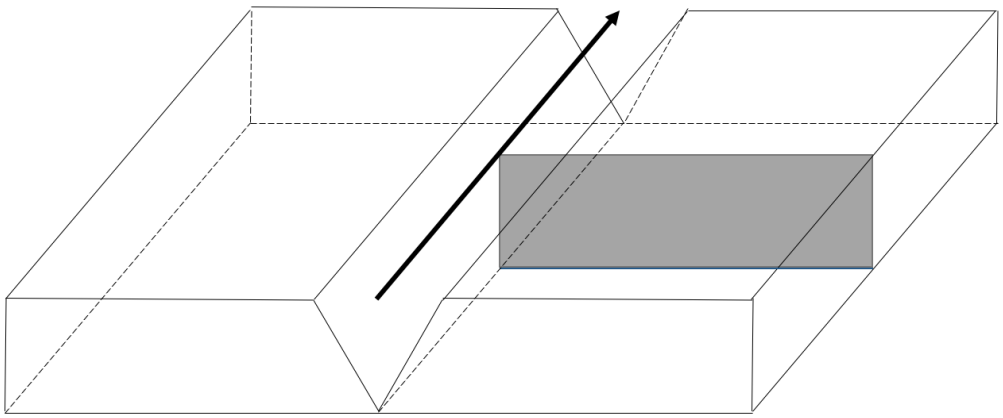

Fig. 1 Gray area represents the modelled area and the arrow indicates the welding direction.

TEMPERATURE MODEL

The heat equation (Eqn. (1)) was solved by using forward-time – centered-space (FTCS) finite difference scheme.

$$\rho c \frac{\partial T}{\partial t} - \nabla \cdot (k \nabla T) = Q \tag{1}$$

BOUNDARY CONDITIONS

The schematics of the boundary conditions used in the simulation are presented in Fig. 2. The boundary condition in all surfaces experiencing air cooling is a combination of convection (Eqn. (2)) and radiation (Eqns. (3) and (4)). Only exemption is that the radiative heat loss in the horizontal direction ($h_{rad,x}$) was assumed to be zero at the groove because the radiation from the opposite hot surface of the groove diminishes the heat loss in this direction. The total heat flux is then calculated by Eqn. (5) [4].

$$h_{conv} = h(T - T_{ext}) \tag{2}$$

$$h_{rad,x} = \cos(\alpha)\sigma\epsilon(T^3 + T^2 T_{ext} + T T_{ext}^2 + T_{ext}^3)(T - T_{ext}) \tag{3}$$

$$h_{rad,y} = \sin(\alpha)\sigma\epsilon(T^3 + T^2 T_{ext} + T T_{ext}^2 + T_{ext}^3)(T - T_{ext}) \tag{4}$$

$$h_{tot} = h_{rad,x} + h_{rad,y} + h_{conv} \tag{5}$$

Symbols in Eqns. (2)-(5) are as follows: σ is the Stefan-Bolzmann's constant, ϵ is the emissivity, h is the convective heat transfer coefficient, T is the absolute temperature at the boundary, the T_{ext} is the ambient temperature in Kelvin and α is the angle between the surface and the y-axis (vertical direction). In this model ϵ and h were taken as 0.75 and 10

$Wm^{-2}K^{-4}$ respectively, following the approach given in Ref. [4]. It was assumed that the filler material is in place at the beginning of each pass. Goldak et al. [1] proposed this as the simplest approach and stated that this would cause error ahead of the weld pool. However, it was assumed that the effect is not as significant in present model, bearing in mind that the model was intended for the heat-affected zone.

Fig. 2 Boundary conditions used in the simulation (during the first pass of two pass weld). The dashed line represents convection and radiation and the solid line seen on the left of the figure represents a symmetry boundary condition.

HEAT INPUT MODEL

Widely used double-ellipsoidal heat source model formulated by Goldak et al. [5] was used as a heat input model. The volumetric heat input to each node was calculated by using Egn. (6) or (7). The term y_0 was added to the heat source model because the global and local y-coordinate may not be the same.

$$Q = \frac{f_f UI\mu 3\sqrt{3}}{ABC_f\pi\sqrt{\pi}} \exp\left(-\frac{3x^2}{A^2} - \frac{3(y-y_0)^2}{B^2} - \frac{3\left(St - C_f\right)^2}{{C_f}^2}\right), St < C_f \tag{6}$$

$$Q = \frac{f_r UI\mu 3\sqrt{3}}{ABC_r\pi\sqrt{\pi}} \exp\left(-\frac{3x^2}{A^2} - \frac{3(y-y_0)^2}{B^2} - \frac{3\left(St - C_f\right)^2}{{C_r}^2}\right), St \geq C_f \tag{7}$$

where Q is the volumetric heat input, x and y are the coordinates of the node, y_0 is the coordinate of the top of the heat source, S is the travel speed and t is time from the beginning of the welding, f_f and f_r are the parameters used to divide equal amount of energy to front and rear quadrant (Eqn. (8)), U is the arc voltage, I is the welding current, A, B, C_f and C_r are the heat source parameters. Parameters A and B are obtained by calculating the area that the consumable will fill and then simply measuring these dimensions as seen in Fig. 3. C_f is equal to the A and C_r is two times the A.

$$f_f = \frac{2C_f}{C_f + C_r}, f_r = \frac{2C_r}{C_f + C_r} \tag{8}$$

The parameters A and B were calculated as follows: First the area of the cross-section of the molten consumable was calculated by Eqn. (9). Then based on the joint preparation and

the area of the bead, the geometric shape of the bead's cross-section was obtained. Finally, based on the shape of the cross-section the parameters were calculated as shown in Fig. 3.

$$A_{bead} = \frac{D_{wire}\pi^2}{4} * \frac{F}{S} \tag{9}$$

where D_{wire} is the diameter of the wire, F is the wire feed rate and S is the travel speed.

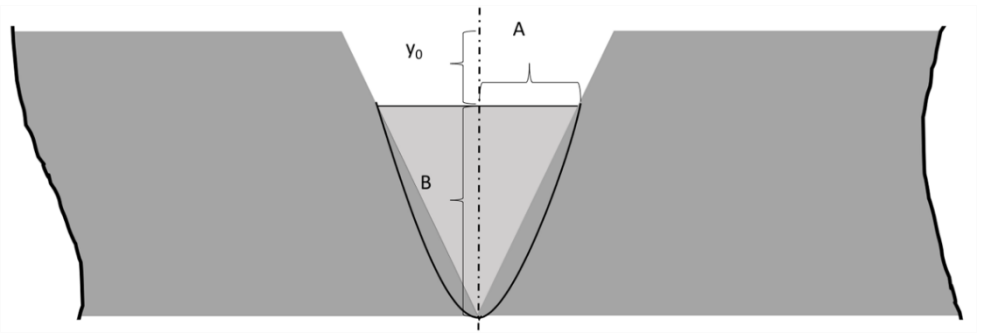

Fig. 3 A schematic showing how the parameters A, B and y_0 are calculated based on the area of the bead.

THERMOPHYSICAL PROPERTIES

In low alloyed steels, density, thermal conductivity and specific heat capacity are highly dependent on the temperature and present phase. Therefore, it is necessary to calculate the properties at each node based on the temperature and phase fractions of that node. In addition, transformation enthalpy of austenite-to-ferrite is temperature dependent. All these properties and their dependence on phase and/or temperature are shown in the Fig. 4.

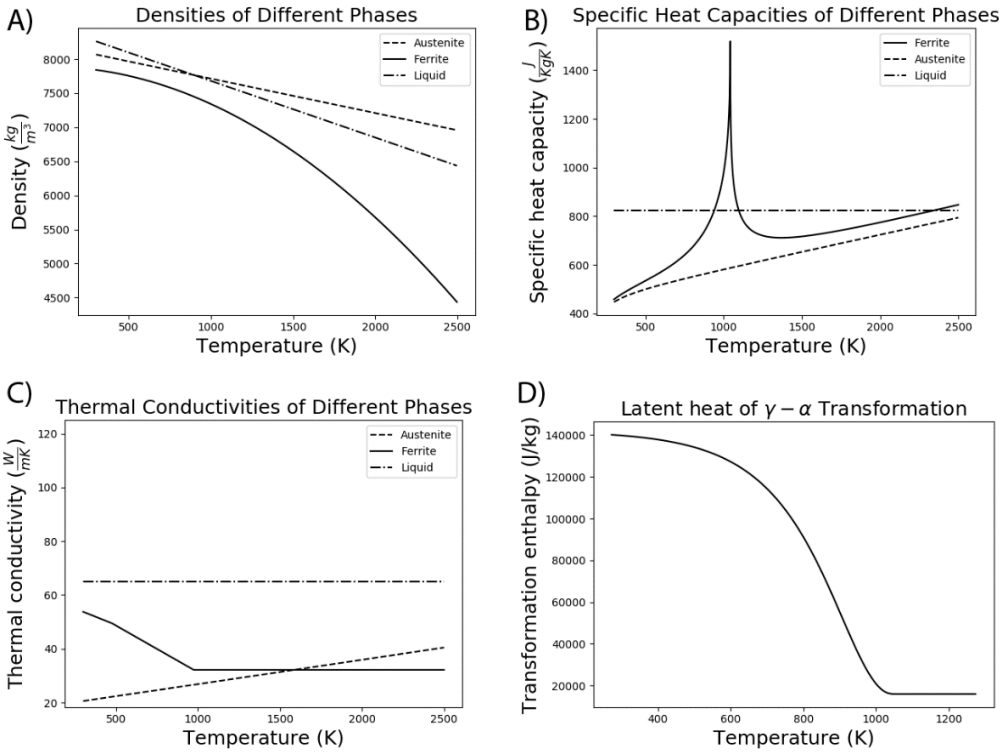

Fig. 4 A) Densities of different phases B) Specific heat capacities of different phases C) Thermal conductivities of different phases D) Latent heat of $\boldsymbol{\gamma - \alpha}$ transformation as a function of temperature

The density of phase mixture was calculated by using Eqn. (10).

$$\rho = 1/\sum \frac{X_i}{\rho_i} \tag{10}$$

where X_i is the volume fraction of the phase i and ρ_i is the density of phase i. Densities of the individual phases are calculated as in Ref. [6].

The specific heat capacity of a phase mixture was calculated by using Eqn. (11)

$$c = \sum c_i X_i \tag{11}$$

where c_i is the specific heat capacity of phase i. Specific heat capacities of ferrite and austenite are calculated as in Ref. [7] and the specific heat capacity of the liquid phase is taken as constant, 825 $Jkg^{-1}K^{-1}$, as presented in Ref. [8].

Finally, the thermal conductivity of phase mixture was calculated by using Eqn. (12)

$$k = \sum k_i X_i \tag{12}$$

where k_i is the thermal conductivity of the phase i. Calculation of the thermal conductivity of austenite and ferrite phase is described in Ref. [6]. Miettinen [6] proposed that thermal conductivity of liquid steel is 35 $Wm^{-1}K^{-1}$ and Watt et al. [2] used 120 $Wm^{-1}K^{-1}$ to simulate the heat transfer by stirring. For this model, a value between these two was chosen i.e. 65 $Wm^{-1}K^{-1}$. The main reason was that the usage of even higher thermal conductivity would add instability to the temperature model if FTCS scheme is used. On the other hand, the low value, 35 $Wm^{-1}K^{-1}$, gave unrealistically high temperatures in the fusion zone.

The latent heat of fusion was taken as constant and it was obtained from Thermo-Calc ® software (TCFE9 database). For steel that was used in the experiments the latent heat of fusion was 275 kJ/kg. The latent heat of fusion includes the transformation heats of the transitory delta-ferrite. The latent heat of austenite-to-ferrite or ferrite-to-austenite transformation can be seen in Fig. 4D [7]. The same value was used also for the austenite-to-bainite and austenite-to-martensite transformations.

MICROSTRUCTURE MODEL

Microstructure model calculates the phase transformations and the grain growth. It also includes a very coarse model for precipitates. Possible phases in phase transformation model are ferrite, bainite, martensite, austenite and liquid. Formation of pearlite was neglected because it was not found in the continuous cooling experiments and thus, it was impossible to find parameters for the formation. As in Ref. [2], the delta-ferrite was omitted from the model. Instead, it is handled as a part of the liquid phase. The reason is that this adds stability to the model because the phase transformations at high temperatures occur presumably in very short time and this combined with the latent heats of transformation is likely to cause instability. In addition, the modelling of the delta-ferrite would require knowledge of the kinetics of austenite to delta-ferrite transformation at high heating rates.

MELTING AND SOLIDIFICATION

Melting and solidification are important phenomena in welding. However, the present model was aimed for HAZ microstructure simulations so the melting and solidification are modelled quite simply. In metals, the melting occurs at the equilibrium melting temperature even at high heating rates [9]. To increase the stability of the model the melting rate is calculated as follows: The melting occurs between solidus (T_S) and liquidus (T_L) temperatures and the rate is $(T_L - T_S)10^{-3}K^{-1}s^{-1}$. The 1000 Ks^{-1} is the approximated heating rate in the fusion zone.

During welding, the nucleation barrier for solidification is very low. Therefore, there is very little undercooling [9]. To avoid the instability caused by latent heat of fusion, the solidification begins only after temperature is 10 degrees below the T_S. It was assumed that

this is within the range of 'very little undercooling'. In reality, the solidifying phase depends on cooling rate [10]. In this model, the solidifying phase is always austenite because, as described previously, the delta-ferrite is combined with the liquid phase.

AUSTENITIZATION

Austenitization kinetics during heating depend on initial microstructure, composition and heating rate. In the experiments it was found that during welding the heating rates are relatively high (~> 80 K/s) in the regions where temperature rises over the A_1 temperature.

The austenitization kinetics were investigated by using the Gleeble thermomechanical simulator (Gleeble® 3800). The test specimens were heated to 1250 °C at heating rates from 10 to 1000 °C/s and the diameter of the specimen was measured by dilatometry and later the change in the diameter was converted to transformed fraction by lever rule. It was found that for the examined low alloyed steel, the austenitization is time-independent on these heating rates. Therefore, the austenitization is modelled rather simply using the Johnson-Mehl-Avrami-Kolmogorov (JMAK) equation that is fitted to the experimental data. While this works very well for the initial microstructure, it remains somewhat questionable how well this represents the austenitization from the microstructure formed after the first pass. The prior austenite grain size in the heat-affected zone of the first pass differs from initial pancaked structure and this may have effect on the transformation rate. The austenitization is modelled by using Eqn. (13)

$$X_A(T) = 1 - \exp(-k\Delta T^n) \tag{13}$$

where X_A is the volume fraction of austenite at temperature T, k and n are parameters fitted to the experimental data, ΔT is the temperature difference between the T and the equilibrium temperature, i.e. A_1 in the intercritical zone and A_3 above that temperature. Note that different values for parameters k and n are used between A_1 and A_3 temperatures and above A_3 temperature.

It is assumed that during austenitization from a mixed microstructure, the initial phases transform into austenite in relation to their volume fractions, for instance, initially 70% bainite – 30 % martensite will be 35% bainite and 15% martensite after 50% of total volume is austenitized.

DECOMPOSITION OF AUSTENITE

During cooling, three different austenite decomposition mechanism are possible and may occur simultaneously. These are the formation of ferrite, bainite and martensite. As noted earlier, the formation of pearlite is neglected because it was not found in experiments, though it could be modelled using the same principles.

Diffusional transformations (austenite to ferrite or bainite) are separated into two parts. The first part is incubation that occurs until the volume fraction of the phase is more than

1%. The second part is nucleation and growth that may occur until austenite is completely decomposed.

The incubation phase is calculated by using Eqns. (14), (15) and (16) following similar approach as in Ref. [11]: The ideal TTT-diagram is obtained from the continuous cooling experiments using the following equation

$$\frac{1}{\tau(\Delta T)} = \frac{d\theta'}{d(\Delta T_{CCT})} \tag{14}$$

where θ' is the constant cooling rate, ΔT_{CCT} is the magnitude of the undercooling at the beginning of the transformation during continuous cooling. According to the Scheil's additivity rule, one percent is transformed when

$$\sum \frac{\Delta t}{\tau(T)} \geq 1 \tag{15}$$

where Δt is the time step and

$$\tau(T) = A_i(T_i - T)^{m_i}\exp(\frac{Q_i}{RT}) \tag{16}$$

where T is the temperature at the beginning of time step, A_i, T_i, m_i and Q_i are parameters fitted for incubation of each phase, separately. After incubation is finished, the phase transformation rate is calculated using Eqn. (17) as presented in Ref. [12].

$$\frac{\Delta X}{\Delta t} = (X_{max} - X)\ln\left(\frac{X_{\max}}{X_{max} - X}\right)^{\frac{n-1}{n}} nk(T)^{1/n} \tag{17}$$

where ΔX is the fraction transformed during one time step (Δt), $X_{\max}$ is the maximum volume fraction of the phase, X is the current volume fraction of the phase, the n is a parameter fitted to experimental data and the k is the rate constant calculated by Eqn. (18) as in Ref. [13].

$$k(T) = exp(a(T - T_0)^2 - c) \tag{18}$$

where a, c and T_0 are parameters fitted to experimental data. For the formation of the bainite, the term presented in Eqn. (19) is added to Eqn. (17). This takes into account the fact that transformation rate is decreased as the austenite is enriched with carbon [14].

$$\frac{C_0}{C_\gamma} \tag{19}$$

where C_0 is the bulk carbon content and

$$C_\gamma = \frac{C_0 - X_f * 0.02}{1.0 - X_f} \tag{20}$$

where X_f is the volume fraction of ferrite that possibly formed before the austenite-to-bainite transformation begun. In addition, the term presented Eqn. (21) is added to Eqn. (17) to take into account the effect of grain size on the formation of ferrite and bainite [2]

$$2^{\frac{G_{current} - G_{parameters}}{2}} \tag{21}$$

where *G* is the ASTM grain size number. Subscripts *current* and *parameters* denotes to the grain size at the moment phase transformation is occurring and the grain size that was in specimens when parameters were obtained, respectively.

For the martensitic transformation, the derivative of Koistinen-Marburger equation (Eqn. (22)) is used as presented in Ref. [4].

$$\frac{\Delta X_m}{\Delta t} = -\mu X_{m,max}\left[1 - \exp\left(-\mu(T_{Ms} - T)\right)\right]\frac{\partial T}{\partial t} + X_m(T = T_{Ms}) \tag{22}$$

where ΔX_m is the transformed volume fraction during one time step (Δt), μ is a coefficient that is fitted to experimental data, T_{Ms} is the martensite start temperature, $X_{m,max}$ is the maximum amount of martensite that may form and the term $X_m(T = T_{Ms})$ takes into account the possibility that there may be already some martensite in the inter-critical zone as the transformation begins.

More detailed description of the austenite decomposition model can be seen in Ref. [15] and result for different steels can be seen in Refs. [15] and [16].

GRAIN GROWTH

As noted above, the prior austenite grain size has an effect on phase transformation kinetics. Therefore, it is important to model the grain growth in austenite. The grain size is also important factor determining the impact toughness of the heat-affected zone and model would also be suitable for indicating if the grain size would be too high. Grain growth during one time step is calculated by using the Eqn. (23)

$$\frac{\Delta D}{\Delta t} = nK\left(\frac{1}{D} - \sum\frac{f}{K_Z r}\right)^{\frac{1}{n}-1} \tag{23}$$

where D is the average grain diameter, K_Z is the Zener coefficient, f is the volume fraction of precipitate and r is the mean particle radius. Zener coefficient is 2.1 for TiN [17] and 4/3 for NbC [9]. Parameters n and K are calculated as in Ref. [17].

Particle pinning is important grain growth controller. Therefore, it is necessary to have reasonable estimation of particle structure during the thermal cycle. In this model, pinning from NbC and TiN particles is taken into account. Volume fraction of the precipitate is estimated during thermal cycle by solving the following integral (Eqn. (24)) numerically [18]

$$f = f_0 \left(1 - \frac{2}{r_0^2} \int_{t_1}^{t_2} \alpha D_m dt\right)^{\frac{3}{2}} \tag{24}$$

where r_0 is the initial particle diameter, D_m is the diffusivity of the less mobile element and α is the ratio between the fraction of the less mobile element in the matrix and in the precipitate. It was assumed that the dissolved particles will not precipitate between two passes but remain in solution. The initial volume fractions of the precipitates were approximated by using Thermo-Calc ® (TFCE9 Database). For the dissolution temperature (T_D) Eqn. (25) was used.

$$T_D = \frac{D}{C - \log[M\%][C\%]} \tag{25}$$

where M and C are the concentrations of metal and non-metal , respectively. The C and D are constants that depend on the precipitate and were taken directly from Ref. [18].

The coarsening of particles is calculated by using Eqn. (26)

$$r^3 = r_0^3 + c_1 \int_{t_1}^{t_2} \frac{1}{T} \exp(-\frac{Q}{RT}) dt \tag{26}$$

where Q is the activation energy for diffusion of the less mobile element, R is the universal gas constant and is c_1 parameter fitted for experimental data [18].

The previous equation for growth is valid only below the equilibrium dissolution temperature. In the present model, it is assumed that precipitates grow below the T_D temperature and the coarsening will not occur simultaneously with the dissolution. Although the precipitation model was not directly verified experimentally, it increased the overall accuracy of the grain growth model significantly. The initial precipitation structure was estimated as follows: the volume fraction of the precipitate was calculated using solubility product. Parameters for solubility product as well as initial particle diameters (5 nm for TiN and 60 nm for NbC) were after Grong [18].

EXPERIMENTAL PROCEDURE

To validate the present model, experimental data was obtained from practical welding trials. Test coupons of 100×120×8 mm were welded to each other by using a Motoman Yasnac RX robot equipped with a Kemppi ProMig 500 gas metal arc welding machine. The chemical composition of the steel is presented in Table 1. The joint preparation was a 50 degree V-groove without a root gap (see Fig. 5A). Four thermocouples were attached on the top surface. The shielding gas was Mison® 25 (Ar + 25%CO_2 + 0.03% NO) with gas flow of 20 l/min. The welding consumable was 1.2 mm Esab OK AristoRod™ 89 solid core wire. Other welding parameters are presented in Table 2.

The welded samples were then cut to 40x8 mm cross-sections, mounted, polished and etched in picric acid for 6 minutes to reveal the prior austenite grain size or in 2% Nital etchant for 10 seconds to reveal the microstructure. The prior austenite grain size (PAGS) was measured using the mean linear intercept method. 400 μm lines were drawn parallel to fusion line and the amount of grain boundary interceptions was calculated. (see Fig. 9D)

Final microstructure characterization was done by using a laser confocal microscope (VK-X200, Keyence Ltd.) to validate the result of the phase transformation model. The phase fractions were calculated by using simple image analysis. A grid of dots was drawn on microstructure images and the amount of dots on each phase were calculated. In case it was not clear what the phase under the dot is it was not taken into consideration. Finally, the phase fractions were estimated by calculating the fraction of the amount of dots per phase and the total amount of calculated dots.

Three welding experiments were carried out and three cross-section specimens were made from each test coupon. However, there was some deviation in the welding current (±10 A) and this had an effect on temperatures. Therefore, the measurements were checked against each other to confirm that there was no significant error in them and then the model was compared with randomly chosen test coupon.

Table 1 Data of the steel used in the experiments

Yield strength (MPa)	C (wt-%)	Mn (wt-%)	Si (wt-%)	Nb+Ti+Mo+Vn (wt-%)	Cr+Ni (wt-%)
960	0.1	1.4	0.3	0.05	1.00

Table 2 Welding parameters

Bead no.	Voltage (V)	Current (A)	Travel speed (cm/min)	Feed rate (m/min)
1	21.9	196	40	5.8
2	22.0	188	50	5.8

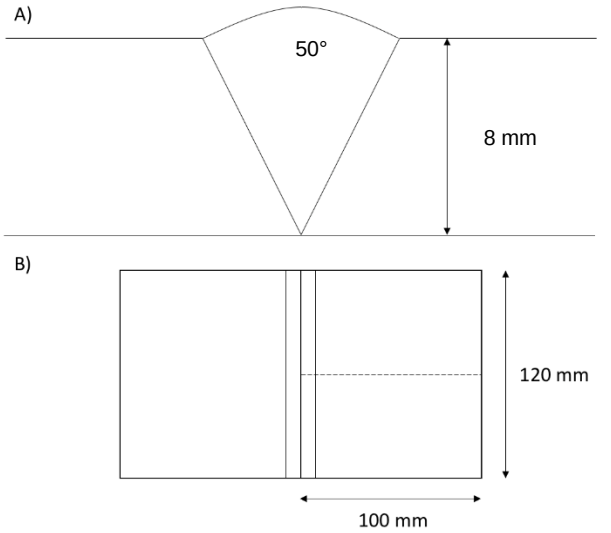

Fig. 5 A) Joint preparation B) Dimensions of the plate. Dashed line represents the line where the thermocouples were attached.

RESULTS AND DISCUSSION

The welding experiment was modelled using the described parameters. The grid spacing in simulations was 0.1 mm and the time step was 0.1 ms. A value of 0.80 was used for the heat input efficiency. This value was chosen because it gave the best correlation between the modelled and measured peak temperatures near the fusion line (5 mm line in Fig. 7). The simulation time was approximately 5 hours. Fig. 6 and Fig. 7 show that there is relatively good agreement between the experimental and modelled results. Evidently, the heat source model is merely an approximation of the complex phenomena in the weld pool and it causes some differences between shapes of the real and modelled fusion zones.

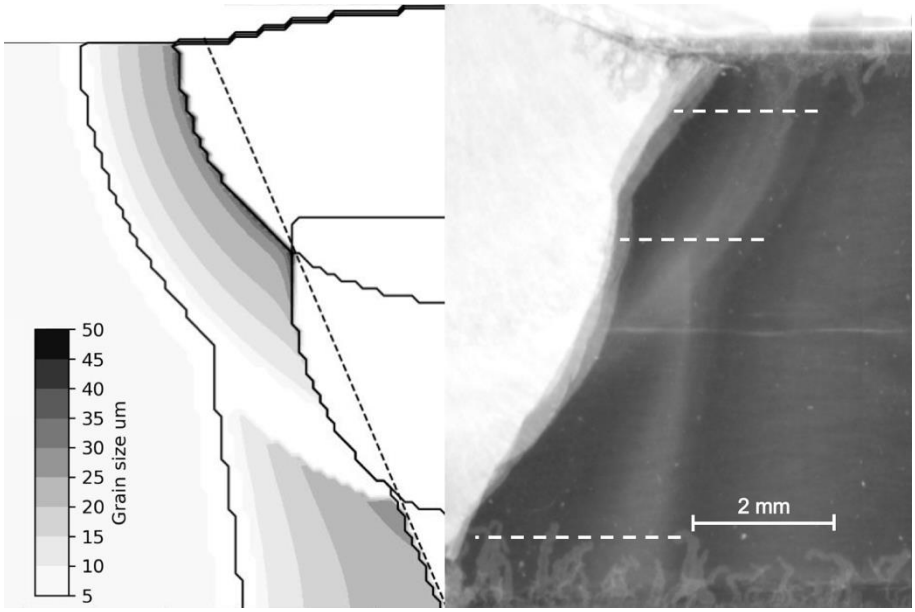

Fig. 6 A figure showing a comparison between a cross-section from the model (left) and a blend of four cross-sections from the practical welding experiments (right). Blending was done due to the fact that the real fusion zones are not perfectly symmetric. Contours in the model image shows the modelled PAGS.

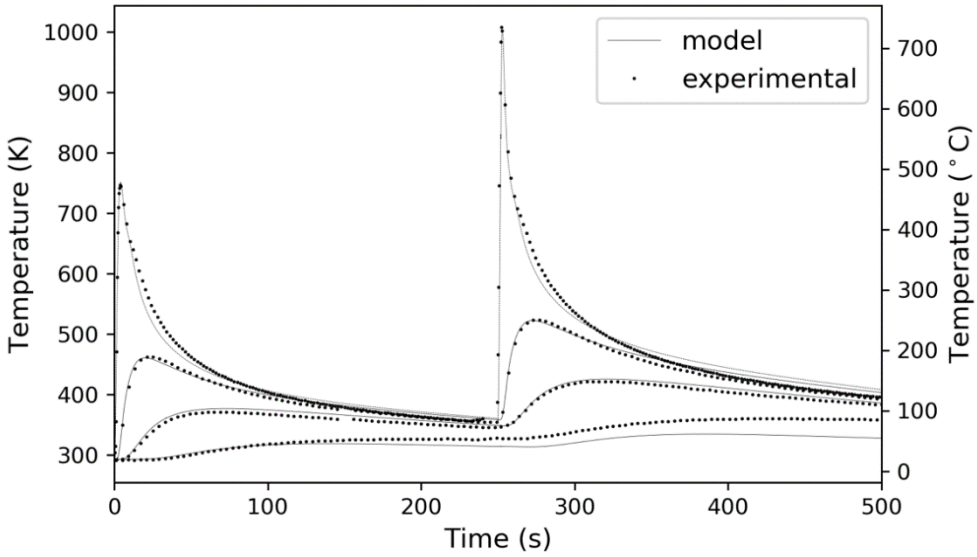

Fig. 7 Temperature curves on the top surface during two-pass welding. Distances of the thermocouples are 5, 20, 40 and 80 mm from the symmetry line on top surface (in decreasing temperature order).

Table 3 Volume fractions from model at the positions presented in Fig. 8

Figure	Bainite model (vol-%)	Bainite exp (vol-%)	Martensite model (vol-%)	Martensite exp (vol-%)
A	95	92	4	8
B	75	80	23	20
C	95	94	4	6
D	80	86	17	14
E	80	93	20	7
F	75	80	24	20

Table 3 shows the comparison between modelled and experimental phase structure. The images are shown in Fig. 8A-F. There is generally a good agreement between these values as the accuracy of the image analysis is approximately ± 15%. The most significant error is in Fig. 8E, which may be due to the fact that the area is tempered during the second pass and that makes the distinguishing of bainite and tempered martensite difficult. In some points, the sum of the phase fractions from the model are not equal to 100%. There are two reason behind this. The volume fraction of ferrite is always at least slightly over zero due to incubation and this may lose one percentage point due to rounding. The model may also propose that there would be some retained austenite. However, the amount of retained austenite may also be numerical error of the phase transformation model.

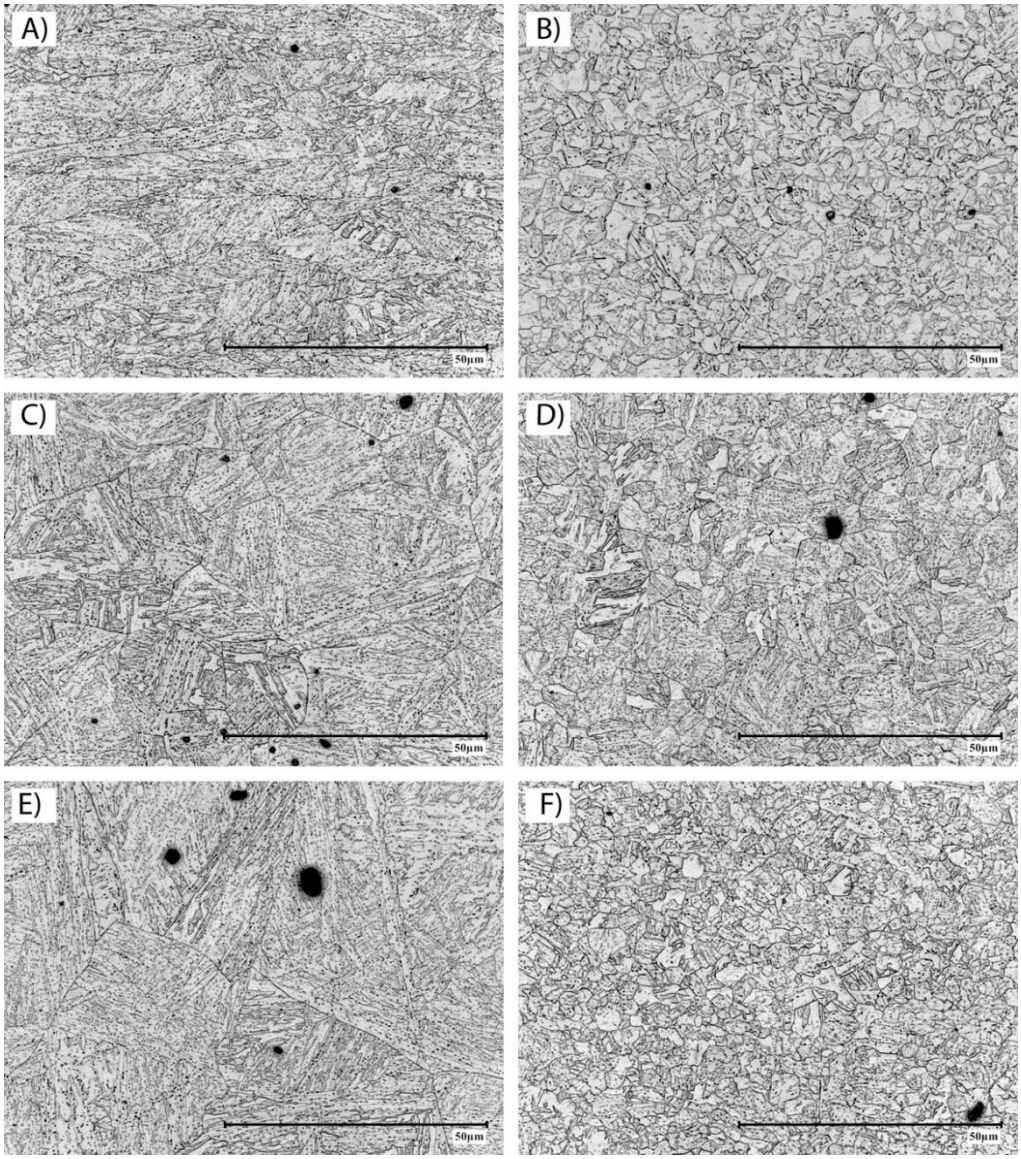

Fig. 8 Microstructure at different areas of the heat-affected zone. Lines referred later are shown in Fig. 6. A) Top line near fusion line. B) Top line near inter-critical zone C) Middle line near fusion line. D) Middle line near inter-critical zone. E) Bottom line near fusion line. F) Bottom line near inter-critical zone.

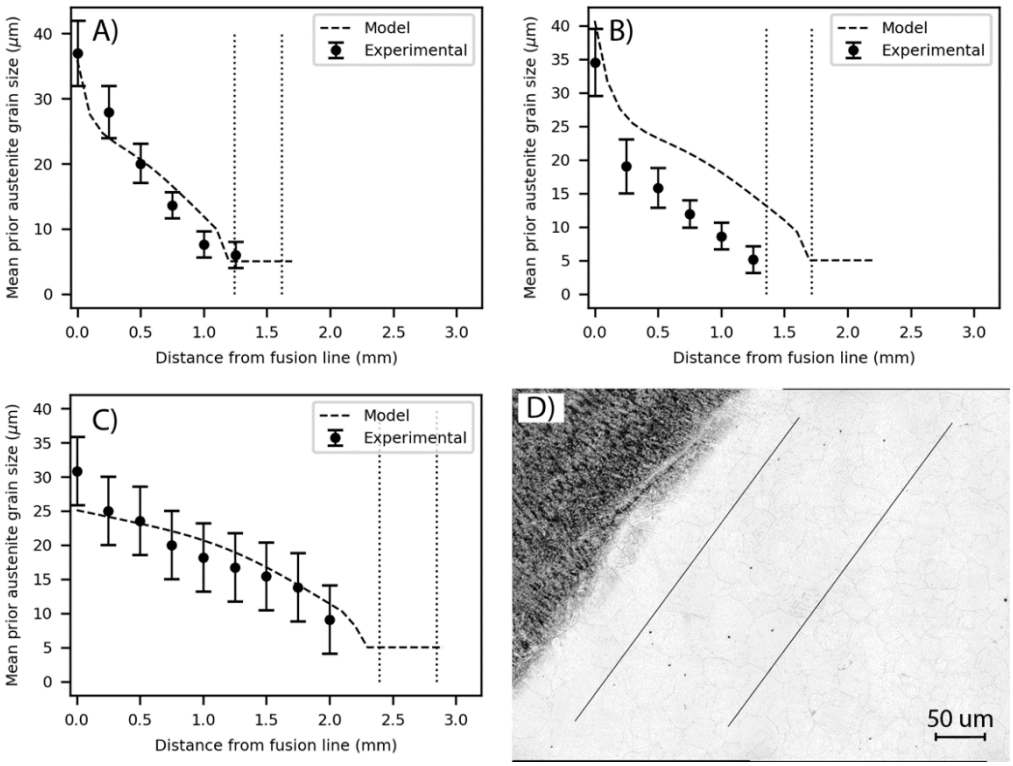

Fig. 9 Mean prior austenite grain size A) near the top surface. B) near the centerline C) near the bottom surface. The grain size of unaffected base material is not shown in the figure and the flat areas in the modelled grain size curves show the inter-critical zone. Dashed vertical line show the real position of the ICHAZ. Lines where the grain sizes were measured from are shown in Fig. 6 D) Image showing how lines were drawn to measure the mean grain size.

The grain growth model seems to work relatively well (Fig. 9A-C). The model predicts a little wider heat-affected zone near the center than is found in actual cross-sections. This indicates that the temperatures have been too high in the model. It is supposed that this is a result from the double-ellipsoidal shape that is not ideal for these types of welds, where the shape of the fusion zone is not perfectly ellipsoidal. In addition, the performance in the initially coarse-grained zone that is partially austenitized during the second pass is very poor and would require more profound model. It is also worth noting that there may be much bigger grains than the average grain size in the coarse-grained zone (abnormal grain growth). Therefore, the grain growth model may not be optimal for situations where the grain size distribution would be needed.

SUMMARY

The model can be used to evaluate the weldability of a steel prior to extensive practical testing because the necessary parameters can be obtained from small specimens. Moreover, model can also aid when finding the proper heat input ranges to produce desired microstructure and properties. It was shown that chosen approach gives reasonable

accuracy in fully austenitizing zones. However, the chosen methods are not necessarily suitable for inter-critical zones and the development of better models for that area would be the topic of future research.

ACKNOWLEDGEMENTS

The authors are grateful to Mr. Juha Uusitalo for the Gleeble experiments and to Mr. Tun Tun Nyo for the valuable help in sample preparation. Also, the authors are grateful for the support of the SSAB Europe Oy.

REFERENCES

[1] J. GOLDAK, M. BIBBY, J. MOORE, R. HOUSE, and B. PATEL: "Computer modeling of heat flow in welds," *Metallurgical Transactions B*, vol. 17, no. 3. pp. 587–600, 1986.

[2] D. F. WATT, L. COON, M. BIBBY, J. GOLDAK, and C. HENWOOD: "An algorithm for modelling microstructural development in weld heat-affected zones (part a) reaction kinetics," *Acta Metall.*, vol. 36, no. 11, pp. 3029–3035, 1988.

[3] C. HENWOOD, M. BIBBY, J. GOLDAK, and D. WATT: "Coupled transient heat transfer-microstructure weld computations (part B)," *Acta Metall.*, vol. 36, no. 11, pp. 3037–3046, 1988.

[4] D. C. MARTIN: "Selected heat conduction problems in thermomechanical treatment of steel," Doctoral Thesis, University of Oulu, 2011.

[5] J. GOLDAK, A. CHAKRAVARTI, and M. BIBBY: "A New Finite Element Model for Welding Heat Sources," *Metallurgical Transactions B*, vol. 15, no. 2. pp. 299–305, 1984.

[6] J. MIETTINEN: "Calculation of solidification-related thermophysical properties for steels," *Metall. Mater. Trans. B*, vol. 28B, pp. 281–297, 1997.

[7] K. M. BROWNE: "Modeling the thermophysical properties of iron and steels," in *Proceedings of materials '98*, 1998, pp. 443–438.

[8] M. BEUTL, G. POTTLACHER, and H. JAGER: "Thermophysical properties of liquid iron," *Int. J. Thermophys.*, vol. 15, no. 6, pp. 1323–1331, 1994.

[9] D. PORTER, K. EASTERLING, and M. SHERIF: *Phase Transformations in Metals and Alloys*, pp.140, 192, 230-231 3rd ed. CRC Press, 2009.

[10] H. K. D. H. BHADESHIA and L. E. SVENSSON: "Modelling the Evolution of Microstructure in Steel Weld Metal," *Math. Model. Weld Phenomena, eds Cerjak, H., Easterling E.K., Inst. Mater. London*, pp. 109–182, 1993.

[11] T. T. PHAM, E. B. HAWBOLT, and J. K. BRIMACOMBE: "Predicting the onset of transformation under noncontinuous cooling conditions: Part II. Application to the Austenite Pearlite Transformation," *Metall. Mater. Trans. A*, vol. 26, no. 8, pp. 1993–2000, 1995.

[12] J. LEBLOND, G. MOTTET, and J. DEVAUX: "Mathematical Models of Anisothermal Phase Transformations in Steels, and Predicted Plastic Behaviour," *Mater. Sci. Technol.*, vol. 1, no. 10, pp. 815–822, 1985.

[13] M. UMEMOTO, K. HORIUCHI, and I. TAMURA: "Pearlite Transformation during Continuous Cooling and Its Relation to Isothermal Transformation," *Trans. Iron Steel Inst. Japan*, vol. 23, no. 8, pp. 690–695, 1983.

[14] B. DONNAY, J. C. HERMAN, V. LEROY, U. LOTTER, R. GROSSTERLINDEN, and H. PIRCHER: "Microstructure evolution of C-Mn steels in the hot-deformation process: the stripcam model," *2nd International Conference on Modelling of Metal Rolling Processes*. pp. 23–35, 1996.

[15] A. POHJONEN, M. SOMANI, and D. PORTER: "Modelling of austenite transformation along arbitrary cooling paths," *Comput. Mater. Sci.*, vol. 150, no. March, pp. 244–251, 2018.

[16] A. POHJONEN, J. PAANANEN, J. MOURUJARVI, T. MANNINEN, J. LARKIOLA, and D. PORTER: "Computer Simulations of Austenite Decomposition of Microalloyed 700 MPa Steel During Cooling," in *Proceedings of 21st international ESAFORM Conference on Material Forming (ESAFORM 2018)*, 2018.

[17] J. MOON, J. LEE, and C. LEE: "Prediction for the austenite grain size in the presence of growing particles in the weld HAZ of Ti-microalloyed steel," *Mater. Sci. Eng. A*, vol. 459, no. 1–2, pp. 40–46, 2007.

[18] O. GRONG: *Metallurgical modelling of welding, second edition*., pp.301-334 London: Institute of Materials, 1997.